

# Multifunctional Superconducting Nanowire Quantum Sensors

Benjamin J. Lawrie,<sup>1,\*</sup> Claire E. Marvinney,<sup>1,†</sup> Yun-Yi Pai,<sup>1</sup> Matthew A. Feldman,<sup>1</sup> Jie Zhang,<sup>1</sup> Aaron J. Miller,<sup>2</sup> Chengyun Hua,<sup>1</sup> Eugene Dumitrescu,<sup>3</sup> and Gábor B. Halász<sup>1</sup>

<sup>1</sup>*Materials Science and Technology Division, Oak Ridge National Laboratory, 1 Bethel Valley Rd, Oak Ridge, TN 37831*

<sup>2</sup>*Quantum Opus LLC, 22241 Roethel Dr Ste A, Novi, MI 48375*

<sup>3</sup>*Computational Science and Engineering Division,*

*Oak Ridge National Laboratory, 1 Bethel Valley Rd, Oak Ridge, TN 37831*

(Dated: September 18, 2021)

Superconducting nanowire single photon detectors (SNSPDs) offer high-quantum-efficiency and low-dark-count-rate single photon detection. In a growing number of cases, large magnetic fields are being incorporated into quantum microscopes, nanophotonic devices, and sensors for nuclear and high-energy physics that rely on SNSPDs, but superconducting devices generally perform poorly in large magnetic fields. Here, we demonstrate robust performance of amorphous SNSPDs in magnetic fields of up to  $\pm 6$  T with a negligible dark count rate and unchanged quantum efficiency at typical bias currents. Critically, we also show that the SNSPD can be used as a magnetometer with sensitivity of better than  $100 \mu\text{T}/\sqrt{\text{Hz}}$  and as a thermometer with sensitivity of  $20 \mu\text{K}/\sqrt{\text{Hz}}$  at 1 K. Thus, a single photon detector integrated into a quantum device can be used as a multifunctional quantum sensor capable of describing the temperature and magnetic field on-chip simply by varying the bias current to change the operating modality from single photon detection to thermometry or magnetometry.

Superconducting nanowire single photon detectors (SNSPDs) offer high speed, high quantum-efficiency, and low dark-count-rate single photon detection [1]. There is an emerging need for SNSPDs capable of operating in large magnetic fields for potential integration with quantum nanophotonic circuits [2–4] and for quantum sensors relevant to nuclear physics [5] and dark matter detection [6–8]. For example, SNSPDs have been integrated with quantum dots in nanophotonic circuits [9], but the development of quantum repeaters or quantum sensors based on coherent interactions with electronic spins in such nanophotonic devices requires high performance operation in magnetic fields [10]. Given the sensitivity of such quantum nanophotonic devices to temperature and field, the ability to locally measure the magnetic field and temperature at the device would also be very appealing, as current experiments generally rely on distinct sensors that may be located centimeters from the location of interest. Further, it has been proposed that axion-like dark matter could be detected with a multi-stack SNSPD placed in a magnetic field via axion-photon coupling [6]. SNSPDs may also enable improved measurements of proton spin polarizability held at low temperatures in large magnetic fields [11, 12]. The ability

to detect photons, magnetic field, and temperature with a single high-sensitivity device in a milliKelvin environment is thus critical to a growing number of quantum technologies spanning nuclear, nanoscale and cosmological physics that rely on photon detection in high field, low temperature environments. In general, SNSPDs do not perform well in large magnetic fields, but some research has demonstrated that small magnetic fields can improve SNSPD performance as described below.

SNSPDs can detect photons when (a) the photon provides enough energy to break an ensemble of Cooper pairs and generate a bath of quasiparticles that form a belt across the width of the nanowire, (b) the photon provides enough energy to unpin a vortex, enabling it to sweep across the nanowire under a Lorentz force, and (c) the photon provides enough energy to form and unbind a vortex-antivortex pair that are swept in opposite directions across the nanowire under a Lorentz force. Field-dependent studies of bright count rates have suggested that vortex motion is the primary detection mechanism in typical NbN SNSPDs [13, 14]. Similar measurements of  $\text{Mo}_x\text{Si}_{1-x}$  SNSPDs with varying wire width have concluded that vortex-antivortex interactions are responsible for bright counts in wide devices made from micron-scale wires while direct quasiparticle belt formation is responsible for bright counts in nanowires of order 100 nm in width [15]. A growing body of literature has made it clear that SNSPDs constructed of different materials with different designs can rely on any of the bright-count mechanisms described above [16].

Dark counts are observed as a result of thermally- or bias-current-induced vortex motion in the absence of any photons, and are generally present even in well shielded detectors operated at 0 T [17, 18]. For  $T \ll T_c$ , the dark counts could also arise from quantum mechanical vortex tunneling events [19]. Because the local vortex

---

\* lawriej@ornl.gov; This manuscript has been authored by UT-Battelle, LLC, under contract DE-AC05-00OR22725 with the US Department of Energy (DOE). The US government retains and the publisher, by accepting the article for publication, acknowledges that the US government retains a nonexclusive, paid-up, irrevocable, worldwide license to publish or reproduce the published form of this manuscript, or allow others to do so, for US government purposes. DOE will provide public access to these results of federally sponsored research in accordance with the DOE Public Access Plan (<http://energy.gov/downloads/doe-public-access-plan>).

† marvinneyce@ornl.gov

pinning potential can be a spatially heterogeneous function of the superconducting film growth conditions and the device geometry, dark counts may arise preferentially from weak spots within the device. Early models suggested that the energy barrier for single vortex crossing is lower than that for phase slips and vortex-antivortex nucleation and annihilation [17] and that vortex-antivortex interactions and phase slips may be ignored, but competing models and measurements have suggested that vortex-antivortex interactions resulting from a Berezinskii-Kosterlitz-Thouless transition are responsible for SNSPD dark counts [20–22].

At high bias currents, hot spots periodically form and disappear at an electrothermal oscillation frequency determined by the device inductance and load impedance [23–27]. The propagation velocity of a normal-superconducting boundary in the nanowire due to Joule heating depends on its critical current [24], which itself has a strong dependence on the applied external magnetic field. While detection events in the electrothermal oscillation regime are a result of a fundamentally different physical process than dark counts detected at lower bias currents, we describe both conventional dark counts and electrothermal oscillations as dark counts in this article for linguistic convenience.

Current crowding at sharp bends can result in a reduced potential barrier for vortex motion and an increased vortex nucleation density. However, external magnetic fields and associated Meissner currents can reduce the effect of current crowding [28, 29]. Early modeling efforts suggested that perpendicular magnetic fields would reduce the critical current for a conventional meander line SNSPD, but small negative perpendicular magnetic fields could increase the critical current of devices patterned in a spiral layout [28]. Other experimental efforts found a slight asymmetry in the dark count rate of TaN and NbN SNSPDs as a function of field [30, 31], consistent with previous modeling [28], subject to the assumption that dark counts originate largely at the sharp corners of the device and allowing for some heterogeneity in the device fabrication [30].

Understanding and controlling vortex motion and hot spot formation in SNSPDs is critical to the development of quantum sensors capable of operating in high magnetic fields, but fully predictive models of single-photon interactions with superconducting nanowires remain a challenge, despite the recent demonstration of a probabilistic criterion for single photon detection based on single vortex motion [32]. Very little work has explored the field dependence of SNSPDs in large magnetic fields, though one recent article did demonstrate that NbN nanowire single photon detectors can be operated in fields as high as 5 T [12], and many researchers have explored the response of superconducting thin films and nanowires in larger magnetic fields [33–39]. Further research is needed to provide an improved understanding of vortex motion in superconducting nanowires and to define the limits of high-field SNSPD operation.

Here, we explore the magnetic field dependence of dark counts and bright counts generated by a commercially available amorphous transition-metal silicide near-infrared SNSPD with a critical temperature of 5 K. Vector magnetic field control allows for a comparison between arbitrary magnetic-field orientations. The 7 nm thick Quantum Opus SNSPD used here has a 70 nm wide meander line with a 50 percent fill fraction that spans an  $11 \times 11 \mu\text{m}$  active area. It was mounted on a printed circuit board (PCB) and suspended in a dilution refrigerator with free-space optical access to the mixing chamber. The device orientation was  $4^\circ$  from parallel to the z-axis of the vector magnet. For most of the data reported here, the z-axis of the vector magnet was swept from -6 to 6 T. Additional measurements were performed with smaller vector fields as a function of field amplitude and direction, with three field orientations with respect to the SNSPD meander line defined in Fig. 3. Data was collected between multiple zero-field cooling sweeps of the device to confirm the repeatability of the results reported here. The SNSPD was heat sunk to the mixing chamber of the dilution refrigerator and the temperature was held at 60 mK unless otherwise specified.

An attenuated 1062 nm CW laser source was delivered to the SNSPD through a free-space optical interface that is described elsewhere [40]. Dark counts were collected with optical access to the dilution refrigerator blocked. All signals were passed through a low frequency filter mounted directly to the SNSPD at the mixing chamber in order to minimize latching and enable high count rate de-

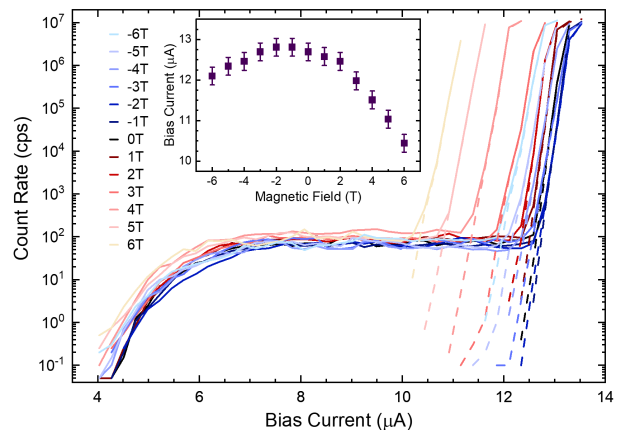


FIG. 1: Measured count rate as a function of bias current and magnetic field for bias currents of 0-14  $\mu\text{A}$  and magnetic fields of -6 to 6 T oriented  $\sim -4^\circ$  from parallel to the film and  $\sim -45^\circ$  from the length of the nanowires. Dark counts (dashed) begin to contaminate the bright count (straight) measurements at bias currents above  $10.0 \mu\text{A}$ . Inset of the bias current at which the dark counts are equal to 10x the plateau bright counts, emphasizing the asymmetry of the field dependence of dark counts at high bias currents.

tection [41]. The bias current and the SNSPD waveforms were delivered along the same semirigid coaxial channel with a room temperature bias tee and low noise amplifiers integrated before time tagging all detection events with a 62 mV threshold. Data was collected (1) continuously for counts as a function of magnetic field for a constant bias current and (2) in 1 T increments for counts as a function of bias current.

The magnetic field dependence of the measured counts is shown as a function of bias current in Fig. 1. At each point on the curve, the bright count rate was averaged for 20 seconds and the dark count rate was averaged for 10 seconds. The relative quantum efficiency of the device remains unchanged, independent of magnetic field, at bias currents within the quantum efficiency plateau of 7.5-9.5  $\mu\text{A}$ . Additionally, the dark count rate was measured to be  $< 0.1$  counts per second within the same 7.5-9.5  $\mu\text{A}$  range for all measured fields. However, as emphasized in the inset of Fig. 1, the maximum operating bias current is suppressed in an asymmetric manner with increasing field, with the maximum operational bias current reduced to  $\sim 10.0$   $\mu\text{A}$  at 6 T, while the maximum operational bias current at -6 T is only reduced to  $\sim 11.5$   $\mu\text{A}$ . A similar, if less pronounced asymmetry is present in the onset of bright count detection events at bias currents of 4-5.5  $\mu\text{A}$  as seen in Fig. 1.

This asymmetric response to changes in magnetic field leads to a decrease in the dark count rate of the device between 0 T and -2.5 T, as shown in Fig. 2. This asymmetry was repeatable for multiple zero-field recoling measurements. The transport properties of the high-count-rate board were also tested separately as a function of parallel field, resulting in no evidence of asymmetry. Thus the asymmetric response shown in Fig. 2 appears to be due to the SNSPD itself.

The data reported in Fig. 2 were acquired in a uni-

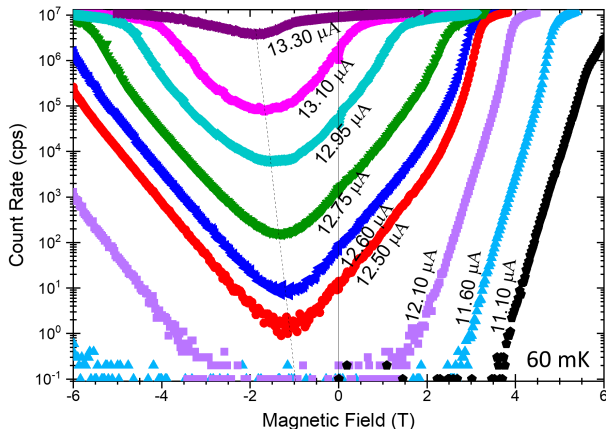


FIG. 2: Dark count rate as a function of field for bias currents of 11.10-13.30  $\mu\text{A}$  at 60 mK. The maximum vector field components of the applied field are 5.980 T (parallel) and 0.420 T (perpendicular).

directional magnetic field where the maximum parallel field was 5.980 T and the maximum perpendicular field was 0.420 T. Experimental constraints did not allow for the device to be mounted in a 6 T parallel field with 0 perpendicular component, but the dark count rate was characterized in smaller fields for different field directions as shown in Fig. 3. The orientations of the applied field with respect to the SNSPD meander line are listed in the caption and inset of Fig. 3 for each of three vector field orientations. For the data represented by blue circles, the field is mostly parallel to the device, with a small perpendicular component; the maximum perpendicular field component is 0.016 T and the maximum parallel field component is 0.222 T. Conversely the red triangles represent data acquired with the field mostly perpendicular to the device, with a small parallel component; the maximum perpendicular field component is 0.238 T and the maximum parallel field component is 0.023 T. The green squares represent a measurement performed in a parallel field. The blue circles are a subset of the 12.60  $\mu\text{A}$  data from Fig. 2. Notably, when perpendicular and parallel field components are both present, the dark count rate appears to scale similarly with the amplitude of the magnetic field. However, in the parallel field represented by the green squares, the dark count rate exhibits a markedly different field dependence. This suggests that the asymmetry of the dark count rate exists only when both perpendicular and parallel field components are present. Experimental constraints limited a full vector field analysis, but simple models consistent with these measurements are presented in the appendices.

Slight asymmetries in the field-dependent SNSPD response have been reported before for mT-scale perpendicular fields and ascribed to magnetic-field induced currents that oppose current crowding effects at the corners of the meander line [28, 30, 31], but the asymmetries reported here rely on similar bias currents but magnetic fields three orders of magnitude larger that have a combination of parallel and perpendicular vector field components. Thus, the previous models for asymmetric SNSPD responses to magnetic fields do not appear to explain this result. Notably, while the onset of bright counts and dark counts is a function of magnetic field, and while the SNSPD waveform can be a function of the photon-nanowire interaction parameters [27, 42], the SNSPD waveforms recorded here were independent of field.

While a detailed model of this field-reversal asymmetry is beyond the scope of this article, we can understand why the asymmetry is much larger than in previous works in the context of the vector magnetic field and symmetry constraints of the meander line. If the top and bottom interfaces of the SNSPD are not identical, as is the case here, a field with a finite component along the long line segments is expected to have a field-reversal asymmetry, and must change sign under current reversal. Indeed, based on the model in Ref. [28], such a field should, depending on its sign, induce current crowding close to the

top or the bottom interface, thus giving different rates for positive and negative fields. Moreover, even if the two interfaces are identical, a field-reversal asymmetry is expected if all three components of the field (parallel to the long line segments, the short line segments, and the perpendicular direction) are finite, as is the case in this work. In contrast, such a field-reversal asymmetry is forbidden for a purely perpendicular field, regardless of whether the top and bottom interfaces are identical or distinct. For a perpendicular field, the asymmetry can then only appear due to imperfections of the meander line [30] or a sufficiently small number of line segments, and it is expected to be much smaller.

The magnetic-field dependence of the dark counts in the high-bias-current regime is intriguing because it suggests that the SNSPD can be utilized as an on-chip magnetometer. For a well characterized SNSPD, monitoring changes in the dark count rate after initially setting the bias current to achieve dark counts of  $\sim 10^2 - 10^6$  cps provides magnetic field sensitivity determined by the slope of the curves shown in Figs 2 and 4 and limited by the uncertainty in counting statistics and bias current. Here, we assume that the field sensitivity can be calculated based on exponential fits to the measured dark counts and that the measured dark counts exhibit Poissonian counting statistics with uncertainty in count rate scaling as  $\sqrt{N}$ . Uncertainty in the bias current source is neglected as a small component relative to the uncertainty in count rate

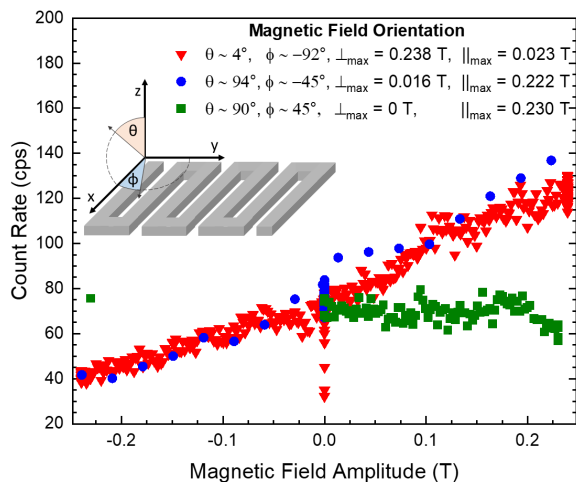


FIG. 3: Field dependence of the dark count rate at a  $12.60 \mu\text{A}$  bias current and  $60 \text{ mK}$  temperature for three vector magnetic field orientations. The inset shows the coordinate system for the magnetic field with respect to the nanowire device. The red triangles represent a largely perpendicular field measurement with small parallel field components, the blue circles represent a largely parallel field measurement with small perpendicular field components, and the green squares represent a parallel field measurement. The blue circles are a subset of the  $12.60 \mu\text{A}$  data from Fig. 2.

due to a measured rms current-noise level of  $40 \text{ pA}$ . Further, uncertainty in photon counting is a fundamental limit that cannot be improved upon for this type of measurement, whereas the uncertainty in bias current can be improved beyond current limits with further engineering.

The maximum sensitivity of the curves shown in Fig. 2 ranges from  $1.8 \text{ mT}/\sqrt{\text{Hz}}$  for a bias current of  $13.3 \mu\text{A}$  at  $-1 \text{ T}$  to  $600 \mu\text{T}/\sqrt{\text{Hz}}$  for a bias current of  $11.10 \mu\text{A}$  at  $6 \text{ T}$ , with the best sensitivity at smaller bias currents closer to the onset of the electrothermal oscillation regime. The best sensitivity measured here was  $75 \mu\text{T}/\sqrt{\text{Hz}}$  for a bias current of  $11.60 \mu\text{A}$  at  $4.8 \text{ T}$ . Thus, the SNSPD can be used as a magnetometer by sweeping the bias current while monitoring the dark count rate to coarsely determine the magnetic field and by monitoring changes in the dark count rate at a constant bias current to track smaller changes in the magnetic field.

Extrapolating the results shown in Fig. 1 to larger fields suggests that a plateau with optimized quantum efficiency and minimized dark counts should still exist for fields as large as  $18 \text{ T}$  and  $-68 \text{ T}$ . It is likely that this extrapolation overestimates the robustness of the SNSPD, as the SNSPD operation relies in part on the description of the SNSPD as a 2D superconductor. For fields above  $6.5 \text{ T}$ , the characteristic length scale  $\sqrt{\hbar/2eB}$  is smaller than the  $7 \text{ nm}$  film thickness, and that description fails [34]. Nonetheless, it is clear from the results in Fig. 1 that the SNSPD is capable of robust operation for fields much larger than  $6 \text{ T}$ .

At higher temperatures, the maximum functional bias current is reduced as thermally induced vortex motion begins to increase, but the same robust high quantum-efficiency, low dark-count-rate operation is observed at all measured fields for bias currents of  $6-12.1 \mu\text{A}$ . As seen in Fig. 4 for dark counts measured at  $\sim 600 \text{ mK}$ , a similar asymmetry is present in the dark count rate, with the minimum dark counts measured for fields between  $-1 \text{ T}$

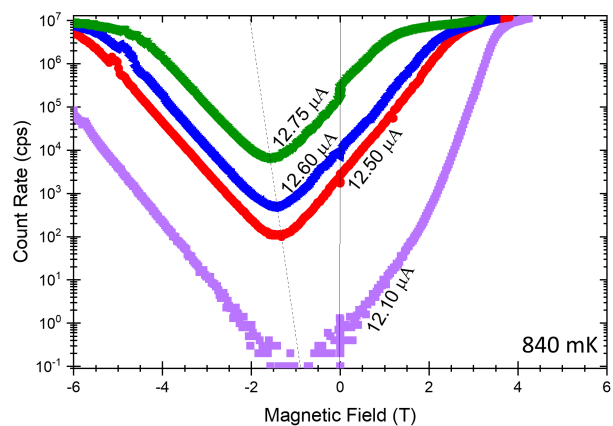


FIG. 4: Dark count rate as a function of field for bias currents of  $12.10-12.75 \mu\text{A}$  at a mixing chamber temperature of  $840 \text{ mK}$ .

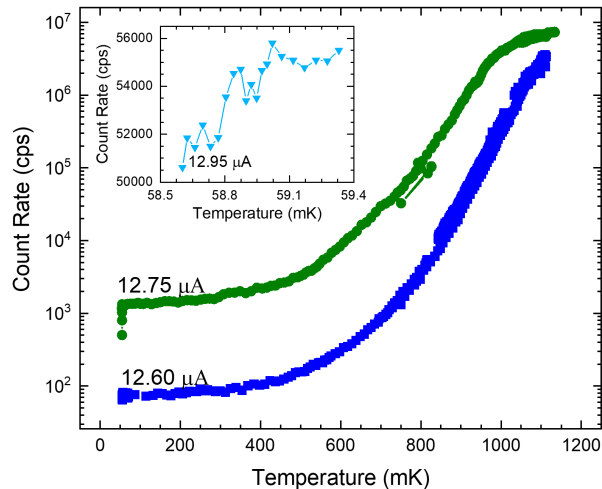


FIG. 5: a) Temperature dependent dark counts for  $12.60 \mu A$  and  $12.75 \mu A$  bias currents at 0 T. The inset illustrates the temperature sensitivity at lower temperatures for a  $12.95 \mu A$  bias current at 0T. b) The mixing chamber thermometer temperature and dark count of the SNSPD at  $12.60 \mu A$  versus time, with inset of the dark count rate tracking with temperature at 1 K.

and -2 T.

Because this SNSPD was mounted to a PCB at a distance of several inches from the nearest thermometer, there is some uncertainty in the SNSPD temperature that would normally be challenging to quantify. However, the dark counts can be used for thermometry just as they can be used for magnetometry. Figure 5 illustrates the measured dark counts for  $12.60 \mu A$  and  $12.75 \mu A$  bias currents at 0 T. As above, the sensitivity of this superconducting nanowire thermometer can be calculated by curve fitting the dark count rate and assuming that the uncertainty in the count rate is limited by the photon counting statistics. The data shown in Fig. 5a illustrate temperature sensitivity of  $20 \mu K/\sqrt{Hz}$  at a temperature of 1 K and a bias of  $12.75 \mu A$ , and a temperature sensitivity of  $45 \mu K/\sqrt{Hz}$  for a  $12.60 \mu A$  current. At 800 mK, the sensitivity is reduced to  $0.1 mK/\sqrt{Hz}$  and  $1.5 mK/\sqrt{Hz}$ , and at 400 mK, the sensitivity is reduced to  $6 mK/\sqrt{Hz}$  and  $40 mK/\sqrt{Hz}$ , respectively at the larger and smaller bias currents. However, further increasing the bias current does continue to increase the sensitivity, and the SNSPD thermometer is most sensitive when the device is operating in the electrothermal oscillation regime with greater than  $10^6$  dark counts per second. With the device operating at a higher bias current, this regime can be reached at lower temperatures, and the onset of the electrothermal oscillations near 100 mK will improve the temperature sensitivity. For example, on the cusp of the electrothermal oscillating regime at 60 mK, the sensitivity is improved to better than  $0.5 mK/\sqrt{Hz}$ , as shown with a bias current of  $12.95 \mu A$  in the inset of

Fig. 5. This improved sensitivity comes at the expense of increasing the device temperature  $\sim 5$  mK at a bias current of  $14 \mu A$ .

The ability to use the SNSPD in large magnetic fields for thermometry or magnetometry in addition to single photon detection is of interest, not just to better quantify the SNSPD operating conditions, but to provide a multifunctional sensor in integrated quantum nanophotonic devices, as described in the introduction. The magnetic field sensitivity recorded here is coarse compared to that of long-established SQUID magnetometer designs[43, 44], but the ability to operate a magnetometer in a large magnetic fields and in an integrated sensing platform offers substantial advantages over SQUID magnetometry. Further, the temperature sensitivity recorded here is competitive with dedicated transition-edge-sensor calorimeters[45]. While the results described in this article provide a device-level understanding of the limitations of thermometry and magnetometry with SNSPDs in large fields, a microscopic understanding of the quasi-particle and vortex interactions that drive this functionality is still needed. Confocal optical microscopies capable of monitoring the SNSPD response as a function of the position and wavelength of incident photons at milliKelvin temperatures and in variable magnetic fields would provide an improved understanding of these interactions at the mesoscale. Additionally, a quantitative model of the magnetic field dependent and temperature dependent electrothermal oscillation frequencies will be pursued as a future work. MilliKelvin scanning probe microscopies including scanning SQUID microscopies [46] and scanning single photon microscopies [40] could help to provide further understanding of these interactions.

## ACKNOWLEDGMENTS

This research was sponsored by the U. S. Department of Energy, Office of Science, Basic Energy Sciences, Materials Sciences and Engineering Division. Postdoctoral (CEM) research support was provided by the Intelligence Community Postdoctoral Research Fellowship Program at the Oak Ridge National Laboratory, administered by Oak Ridge Institute for Science and Education through an interagency agreement between the U.S. Department of Energy and the Office of the Director of National Intelligence. Student (MAF, BEL) research support were provided by the Department of Defense through the National Defense Science & Engineering Graduate Fellowship (NDSEG) and by the DOE Science Undergraduate Laboratory Internships (SULI) program.

## APPENDIX

### 1. Possible origin of magnetic field dependent dark count rate

To understand the impact of vortex crossing (VC) dynamics on our measured dark counts we follow the current-dependent phenomenological model proposed in Ref. [47]:

$$R_{VC} \approx R_0 \exp\left(\frac{I_b}{\tilde{I}}\right) \quad (\text{A1})$$

where  $R_0$  is a proportionality factor and  $\tilde{I}$  scales with the experimental critical current,  $I_c$ . The fit of our data to Eq. (A1) in Fig. 6(a) shows that this is a satisfactory description of the current dependence of  $R_{VC}$ . Here we treat  $R_0$  and  $\tilde{I}$  as fitting parameters.

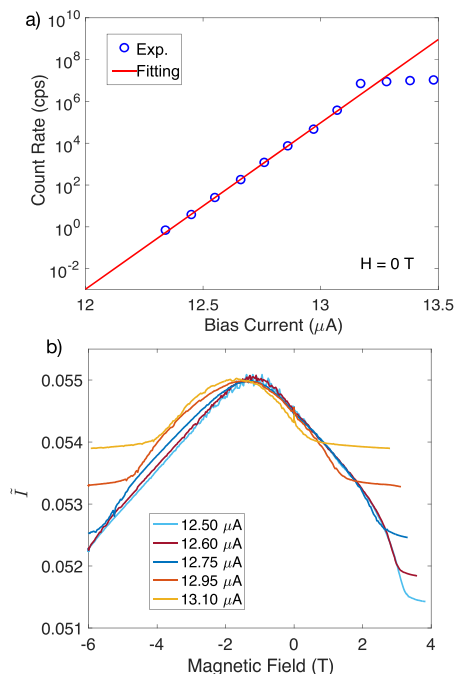


FIG. 6: (a) Measured dark counts as a function of bias currents at zero field (circles). The solid line is a least squares fit to the phenomenological model given by Eq. (A1). (b) Extracted  $\tilde{I}$  as a function of the applied magnetic field at various bias currents.

The measured dark count rate as a function of the applied magnetic field  $H$  given in Fig. 2 of the main text clearly showed a magnetic-field dependence with an asymmetry with respect to the field direction. References [47] and [48] discussed the effect of an applied magnetic field on the rate of vortex crossings (without photons) and determined that the imperfections from the meander line structure might cause the asymmetric dependence of dark counts on the applied field. To identify the critical current for which the barrier for vortex entry vanishes

while keeping the model as simple as possible, we assume the current scale,  $\tilde{I}$ , in Eq. (A1) is the only magnetic-field dependent parameter in the model. Such an assumption allows us to extract the dependence of critical current on the magnetic field from the measured dark count data given in Fig. 2 of the main text. In Fig. 6(b) we plot the extracted  $\tilde{I}$  as a function of the applied field magnitude at a given bias current. Surprisingly,  $\tilde{I}(H)$  at different bias currents collapses on top of each other, which suggests that the asymmetric dependence on the applied field might be solely caused by the critical current. In Appendix 2, we propose an argument based on symmetry constraints to explain the asymmetric dependence of the critical current on the applied field.

Besides vortex crossing, we also explore the possibility of VAP unbinding contributing to dark counts. According to Ref. [49] and [50], the dark count rate due to VAP unbinding is expressed as  $R_{VAP} = R_0 \exp(-U_{VAP}/k_B T)$  with a proportionality factor  $R_0$  and the Boltzmann constant  $k_B$ .  $U_{VAP}$  is the potential at the saddle point expressed as [50],

$$U_{VAP} = 2(\gamma A - k_B T \ln N_0) + \frac{A}{\epsilon} \left[ \ln\left(\frac{2.6 I_c}{I_b}\right) + \frac{I_b}{2.6 I_c} - 1 \right], \quad (\text{A2})$$

where  $\gamma$  is a temperature and magnetic field independent constant,  $N_0$  is a measure of the number of independent configurations [51], and  $\epsilon$  is the dielectric constant depending on the density of the VAP. Here,  $A = \Phi_0^2 / (\pi \mu_0 \Lambda)$ , where  $\Phi_0$  is the flux quantum,  $\mu_0$  the permeability, and  $\Lambda = 2\lambda^2/d$  the effective penetration depth. Note that  $A$  only depends on temperature and is independent of the applied magnetic field. Assuming  $\lambda \sim 100$  nm,  $\epsilon \sim 1$ , and  $T \sim 100$  mK,  $A/\epsilon \sim 3 \times 10^5$  when normalized by  $k_B T$ . In contrast, a least squares fit of Eq. (A2) to the measured dark count rate as a function of bias current at zero field gives  $A/\epsilon \sim 100$  times smaller than this calculated value. Therefore, we conclude that VAP unbinding is not the dominant source of dark counts in our device.

### 2. Symmetry constraints on the magnetic-field asymmetry

We consider a SNSPD meander line carrying an electrical current  $I$  (see Fig. 7). The three coordinate axes are parallel to the short line segments ( $a$ ), the long line segments ( $b$ ), and the out-of-plane direction ( $c$ ), respectively. If the meander line is infinitely long and has no imperfections, its symmetry group is generated by three symmetry operations: the mirror reflection across the plane of the meander line ( $M_c$ ), the mirror reflection across the center of a short line segment ( $M_a$ ), as well as the combination of the mirror reflection across the center of a long line segment and the translation in the  $a$  direction by the length of a short line segment ( $\tilde{M}_b = M_b \circ T_a$ ). Under these three symmetry operations, the magnetic field

$\vec{H} = (H_a, H_b, H_c)$  and the electrical current  $I$  carried by the meander line transform according to

$$\begin{aligned} M_c &: (H_a, H_b, H_c) \rightarrow (-H_a, -H_b, H_c), & I &\rightarrow I, \\ M_a &: (H_a, H_b, H_c) \rightarrow (H_a, -H_b, -H_c), & I &\rightarrow -I, \\ \tilde{M}_b &: (H_a, H_b, H_c) \rightarrow (-H_a, H_b, -H_c), & I &\rightarrow I. \end{aligned} \quad (\text{A3})$$

Importantly, the operations  $M_c$  and  $\tilde{M}_b$  preserve the direction of the current while  $M_a$  reverses the direction of the current. Thus, the former two operations can be used to establish the symmetry constraints on the field asymmetry for a given current, while the latter operation can be used to determine how the field asymmetry behaves under current reversal. If the dark-count rate for a field  $\vec{H} = (H_a, H_b, H_c)$  is given by  $N(H_a, H_b, H_c)$ , the current-preserving operations  $M_c$ ,  $\tilde{M}_b$ , and  $M_c \circ \tilde{M}_b$  readily imply

$$\begin{aligned} N(H_a, H_b, H_c) &= N(-H_a, -H_b, H_c) = \\ N(-H_a, H_b, -H_c) &= N(H_a, -H_b, -H_c). \end{aligned} \quad (\text{A4})$$

Therefore, a field asymmetry is forbidden if at least one component of the field vanishes and only allowed if all three components are finite. If the dark-count rate for the same field and a reversed current is  $N'(H_a, H_b, H_c)$ , the current-reversing operation  $M_a$  and the current-preserving operation  $\tilde{R}_a = M_c \circ \tilde{M}_b$  can be used to establish

$$\begin{aligned} N'(H_a, H_b, H_c) &\stackrel{M_a}{=} N(H_a, -H_b, -H_c) \\ &\stackrel{\tilde{R}_a}{=} N(H_a, H_b, H_c). \end{aligned} \quad (\text{A5})$$

Therefore, the field asymmetry remains the same under current reversal. Assuming that the field asymmetry is linear in the field, its simplest dependence on the field components that is consistent with the above symmetry

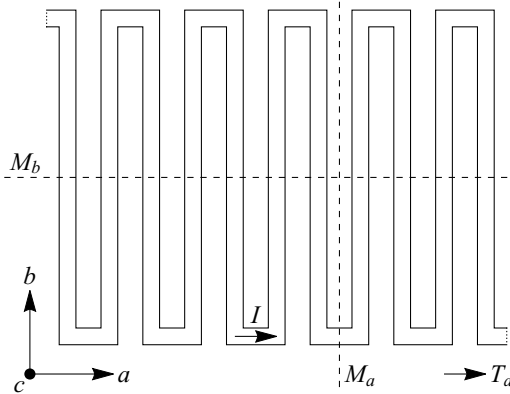


FIG. 7: Illustration of an infinitely long meander line carrying an electrical current  $I$ , along with three coordinate axes  $a, b, c$ , the reflection symmetry axes  $M_a$  and  $M_b$  and the translation symmetry axis  $T_a$  whose combination  $\tilde{M}_b = M_b \circ T_a$  is another symmetry.

considerations is

$$\begin{aligned} \delta N(H_a, H_b, H_c) &\equiv \\ N(H_a, H_b, H_c) - N(-H_a, -H_b, -H_c) &= \\ &= \frac{\alpha H_a H_b H_c}{H^2}, \end{aligned} \quad (\text{A6})$$

where  $H \equiv |\vec{H}|$ , and  $\alpha$  is an undetermined coefficient. While it is not clear what kind of microscopic mechanism could give rise to such a field asymmetry, we can immediately deduce that this mechanism would need to break time-reversal symmetry. Under a time-reversal operation  $\Theta$ , the current and the field are both reversed:

$$\Theta : (H_a, H_b, H_c) \rightarrow (-H_a, -H_b, -H_c), \quad I \rightarrow -I. \quad (\text{A7})$$

In the presence of time-reversal symmetry, the time-reversal operation  $\Theta$  and the other current-reversing operation  $P = M_a \circ \tilde{R}_a$  (which is an inversion) can then be used to establish

$$\begin{aligned} N(H_a, H_b, H_c) &\stackrel{\Theta}{=} N'(-H_a, -H_b, -H_c) \\ &\stackrel{P}{=} N(-H_a, -H_b, -H_c), \end{aligned} \quad (\text{A8})$$

which means that a field asymmetry is forbidden for any direction of the field. In other words, any field asymmetry for a perfect and infinitely long meander line must result from a microscopic mechanism that breaks time-reversal symmetry by involving some dissipative process, for example, the viscous drag force for a superconducting vortex.

If the meander line contains enough imperfections or a sufficiently small number of line segments, the operations  $M_a$  and  $\tilde{M}_b$  are no longer symmetries of the meander line. In this case, the only remaining symmetry operation is  $M_c$  and, according to Eq. (A3), a field asymmetry is allowed if and only if the field has a finite out-of-plane component ( $H_c$ ). The simplest form of the corresponding field asymmetry is then given by  $\delta N(H_a, H_b, H_c) = \beta H_c$ , where  $\beta$  is an undetermined coefficient. This case has been discussed extensively in the literature; if the left and right turns of the meander line have different numbers or are not entirely equivalent, a field asymmetry results from statistically stronger current crowding at the inner (outer) corners for one sign (the other sign) of  $H_c$ . Since this mechanism respects time-reversal symmetry, the corresponding field asymmetry must change sign under current reversal (as the time-reversal operation  $\Theta$  simultaneously reverses the field and the current).

If instead the meander line has different top and bottom interfaces, the operation  $M_c$  is no longer a symmetry of the meander line. In this case, the only current-preserving symmetry operation is  $\tilde{M}_b$  and, according to Eq. (A3), a field asymmetry is allowed if and only if the field has a finite component parallel to the long line segments ( $H_b$ ). The simplest form of the corresponding field asymmetry is then given by  $\delta N(H_a, H_b, H_c) = \gamma H_b$ , where  $\gamma$  is an undetermined coefficient. This field asymmetry may result from current crowding at the top (bottom) interface for one sign (the other sign) of  $H_b$ . Once

again, since this mechanism respects time-reversal symmetry, the corresponding field asymmetry must change sign under current reversal. Experimental constraints

prevented tests of changes in asymmetry under current reversal, but such measurements would provide a straightforward test of this model.

- 
- [1] C. M. Natarajan, M. G. Tanner, and R. H. Hadfield, *Superconductor Science and Technology* **25**, 063001 (2012).
- [2] S. Khasminskaya, F. Pyatkov, K. Slowik, S. Ferrari, O. Kahl, V. Kovalyuk, P. Rath, A. Vetter, F. Hennrich, M. M. Kappes, *et al.*, *Nature Photonics* **10**, 727 (2016).
- [3] C. E. Dreyer, A. Alkauskas, J. L. Lyons, A. Janotti, and C. G. Van de Walle, *Annual Review of Materials Research* **48**, 1 (2018).
- [4] P. Rath, O. Kahl, S. Ferrari, F. Sproll, G. Lewes-Malandrakis, D. Brink, K. Ilin, M. Siegel, C. Nebel, and W. Pernice, *Light: Science & Applications* **4**, e338 (2015).
- [5] H. Azzouz, S. N. Dorenbos, D. De Vries, E. B. Ureña, and V. Zwiller, *AIP Advances* **2**, 032124 (2012).
- [6] K. K. Berggren, *SnowMass* (2021).
- [7] J. A. JPL, J. Chiles, B. K. JPL, A. Lita, J. Luskin, S. W. Nam, M. S. JPL, V. Verma, and E. W. JPL, *SnowMass* (2021).
- [8] Y. Hochberg, I. Charaev, S.-W. Nam, V. Verma, M. Colangelo, and K. K. Berggren, *Physical Review Letters* **123**, 151802 (2019).
- [9] R. Gourgues, I. E. Zadeh, A. W. Elshaari, G. Bulgarini, J. W. Los, J. Zichi, D. Dalacu, P. J. Poole, S. N. Dorenbos, and V. Zwiller, *Optics Express* **27**, 3710 (2019).
- [10] D. Chen, N. Zheludev, and W.-b. Gao, *Advanced Quantum Technologies* **3**, 1900069 (2020).
- [11] T. Polakovic, W. Armstrong, G. Karapetrov, Z.-E. Meziani, and V. Novosad, *Nanomaterials* **10**, 1198 (2020).
- [12] T. Polakovic, W. Armstrong, V. Yefremenko, J. Pearson, K. Hafidi, G. Karapetrov, Z.-E. Meziani, and V. Novosad, *Nuclear Instruments and Methods in Physics Research Section A: Accelerators, Spectrometers, Detectors and Associated Equipment* **959**, 163543 (2020).
- [13] D. Y. Vodolazov, Y. P. Korneeva, A. Semenov, A. Korneev, and G. Goltzman, *Physical Review B* **92**, 104503 (2015).
- [14] R. Lusche, A. Semenov, Y. Korneeva, A. Trifonov, A. Korneev, G. Gol'tsman, and H.-W. Hübers, *Physical Review B* **89**, 104513 (2014).
- [15] Y. P. Korneeva, N. Manova, I. Florya, M. Y. Mikhailov, O. Dobrovolskiy, A. Korneev, and D. Y. Vodolazov, *Physical Review Applied* **13**, 024011 (2020).
- [16] A. Engel, J. Lonsky, X. Zhang, and A. Schilling, *IEEE Transactions on Applied Superconductivity* **25**, 1 (2014).
- [17] L. Bulaevskii, M. Graf, C. Batista, and V. Kogan, *Physical Review B* **83**, 144526 (2011).
- [18] L. N. Bulaevskii, M. J. Graf, and V. G. Kogan, *Physical Review B* **85**, 014505 (2012).
- [19] F. Tafuri, J. Kirtley, D. Born, D. Stornaiuolo, P. Medaglia, P. Orgiani, G. Balestrino, and V. Kogan, *EPL (Europhysics Letters)* **73**, 948 (2006).
- [20] T. Yamashita, S. Miki, K. Makise, W. Qiu, H. Terai, M. Fujiwara, M. Sasaki, and Z. Wang, *Applied Physics Letters* **99**, 161105 (2011).
- [21] A. Engel, A. Semenov, H.-W. Hübers, K. Ilin, and M. Siegel, *Physica C: Superconductivity and its applications* **444**, 12 (2006).
- [22] J. Kitaygorsky, I. Komissarov, A. Jukna, D. Pan, O. Minaeva, N. Kaurova, A. Divochiy, A. Korneev, M. Tarkhov, B. Voronov, *et al.*, *IEEE Transactions on Applied Superconductivity* **17**, 275 (2007).
- [23] R. Hadfield, A. J. Miller, S. W. Nam, R. L. Kautz, and R. E. Schwall, *Applied Physics Letters* **87**, 203505 (2005).
- [24] A. J. Kerman, J. K. Yang, R. J. Molnar, E. A. Dauler, and K. K. Berggren, *Physical Review B* **79**, 100509 (2009).
- [25] D. Liu, L. You, S. Chen, X. Yang, Z. Wang, Y. Wang, X. Xie, and M. Jiang, *IEEE transactions on applied superconductivity* **23**, 2200804 (2013).
- [26] K. K. Berggren, Q.-Y. Zhao, N. Abebe, M. Chen, P. Ravindran, A. McCaughan, and J. C. Bardin, *Superconductor Science and Technology* **31**, 055010 (2018).
- [27] C. E. Marvinney, B. E. Lerner, A. A. Puretzy, A. J. Miller, and B. J. Lawrie, *Superconductor Science and Technology* **34**, 035020 (2021).
- [28] J. R. Clem, Y. Mawatari, G. Berdiyrov, and F. Peeters, *Physical Review B* **85**, 144511 (2012).
- [29] K. Ilin and M. Siegel, *Physica C: Superconductivity and its Applications* **503**, 58 (2014).
- [30] A. Engel, A. Schilling, K. Il'in, and M. Siegel, *Physical Review B* **86**, 140506 (2012).
- [31] I. Charaev, A. Semenov, K. Ilin, and M. Siegel, *IEEE Transactions on Applied Superconductivity* **29**, 1 (2019).
- [32] S. Jahani, L.-P. Yang, A. Buganza Tepole, J. C. Bardin, H. X. Tang, and Z. Jacob, *Journal of Applied Physics* **127**, 143101 (2020).
- [33] H. J. Gardner, A. Kumar, L. Yu, P. Xiong, M. P. Warusawithana, L. Wang, O. Vafek, and D. G. Schlom, *Nature physics* **7**, 895 (2011).
- [34] R. Rosenbaum, *Phys. Rev. B* **32**, 2190 (1985).
- [35] V. Rouco, C. Navau, N. Del-Valle, D. Massarotti, G. P. Papari, D. Stornaiuolo, X. Obradors, T. Puig, F. Tafuri, A. Sanchez, *et al.*, *Nano letters* **19**, 4174 (2019).
- [36] R. Córdoba, T. Baturina, J. Sesé, A. Y. Mironov, J. De Teresa, M. Ibarra, D. Nasimov, A. Gutakovskii, A. Latyshev, I. Guillamón, *et al.*, *Nature communications* **4**, 1 (2013).
- [37] N. Samkharadze, A. Bruno, P. Scarlino, G. Zheng, D. DiVincenzo, L. DiCarlo, and L. Vandersypen, *Physical Review Applied* **5**, 044004 (2016).
- [38] X. Zhang, A. Engel, Q. Wang, A. Schilling, A. Semenov, M. Sidorova, H.-W. Hübers, I. Charaev, K. Ilin, and M. Siegel, *Physical Review B* **94**, 174509 (2016).
- [39] H. Bao, T. Xu, C. Li, X. Jia, L. Kang, Z. Wang, Y. Wang, X. Tu, L. Zhang, Q. Zhao, *et al.*, *IEEE Transactions on Applied Superconductivity* **31**, 1 (2021).
- [40] B. J. Lawrie, M. Feldman, C. E. Marvinney, and Y.-Y. Pai, in *Quantum Nanophotonic Materials, Devices, and Systems 2021*, Vol. 11806 (International Society for Optics and Photonics, 2021) p. 1180604.

- [41] A. Miller and T. Rambo, “Noise suppressing interface circuit for device with control circuits in different noise environments,” (2020), US Patent App. 16/399,207.
- [42] C. Cahall, K. L. Nicolich, N. T. Islam, G. P. Lafyatis, A. J. Miller, D. J. Gauthier, and J. Kim, *Optica* **4**, 1534 (2017).
- [43] F. Wellstood, C. Heiden, and J. Clarke, *Review of scientific instruments* **55**, 952 (1984).
- [44] V. Bouchiat, *Superconductor Science and Technology* **22**, 064002 (2009).
- [45] D. Goldie, K. Rostem, and S. Withington, *Journal of Applied Physics* **108**, 014505 (2010).
- [46] L. Ceccarelli, D. Vasyukov, M. Wyss, G. Romagnoli, N. Rossi, L. Moser, and M. Poggio, *Physical Review B* **100**, 104504 (2019).
- [47] A. Engel, A. Schilling, K. Il'in, and M. Siegel, *Physical Review B* **86**, 140506 (2012).
- [48] L. N. Bulaevskii, M. J. Graf, and V. G. Kogan, *Physical Review B* **85**, 014505 (2012).
- [49] T. Yamashita, S. Miki, K. Makise, W. Qiu, H. Terai, M. Fujiwara, M. Sasaki, and Z. Wang, *Applied Physics Letters* **99**, 161105 (2011).
- [50] A. Engel, A. Semenov, H.-W. Hbers, K. Ilin, and M. Siegel, *Physica C: Superconductivity and its Applications* **444**, 12 (2006).
- [51] J. E. Mooij, in *Percolation, Localization, and Superconductivity*, edited by A. M. Goldman and S. A. Wolf (Springer US, 1984) pp. 325–370.